Research Article | Vol. 13, No. 11 / 1 Nov 2022 / Biomedical Optics Express 5860
Biomedical Optics EXPRESS

Ultrahigh-speed multimodal adaptive optics system for microscopic structural and functional imaging of the human retina

ZHUOLIN LIU,[1,*] FURU ZHANG,[1,,2] KELVY ZUCCA,[1] ANANT AGRAWAL,[1] AND DANIEL X. HAMMER[1]

[1] *Center for Devices and Radiological Health (CDRH), U. S. Food and Drug Administration (FDA), Silver Spring, Maryland 20993, USA*
[2] *Co-first author*
[*] *Zhuolin.Liu@fda.hhs.gov*

Abstract: We describe the design and performance of a multimodal and multifunctional adaptive optics (AO) system that combines scanning laser ophthalmoscopy (SLO) and optical coherence tomography (OCT) for simultaneous retinal imaging at 13.4 Hz. The high-speed AO-OCT channel uses a 3.4 MHz Fourier-domain mode-locked (FDML) swept source. The system achieves exquisite resolution and sensitivity for pan-macular and transretinal visualization of retinal cells and structures while providing a functional assessment of the cone photoreceptors. The ultra-high speed also enables wide-field scans for clinical usability and angiography for vascular visualization. The FDA FDML-AO system is a powerful platform for studying various retinal and neurological diseases for vision science research, retina physiology investigation, and biomarker development.

1. Introduction

Adaptive optics (AO) is a technology that senses and corrects optical aberrations induced in a target to achieve high resolution, near diffraction-limited images of that target. In ophthalmology, ocular aberrations arising primarily from the tear film, cornea, and lens degrade retinal images idiosyncratically, requiring an imaging device to actively adapt in real-time for personalized correction [1]. AO was successively integrated into conventional fundus imaging (i.e., flood illumination-detection ophthalmoscopy) [2], confocal scanning laser ophthalmoscopy (SLO) [3], and optical coherence tomography (OCT) [4] to achieve cellular-level performance [1,5–8]. AO has been successfully used to demonstrate resolution of cells and structures throughout the lamellar retina in the living human, first relatively large and bright cells/structures such as wave-guiding cone photoreceptors [2], nerve fiber bundles [9], and retinal vasculature [10]; and then smaller, transparent, or difficult to localize cells/structures including rod photoreceptors [11], the monolayered retinal pigment epithelium (RPE) [12–15], transparent ganglion cells in the inner retina [16], immune cells [17–19], and the dense choriocapillaris [20,21]. Along the way novel AO-SLO detection methods have been implemented for signal enhancement, notably single and multiphoton fluorescence techniques demonstrated in non-human primates, to probe retinal molecular activity [22,23], and non-confocal split detection approaches that use multiply scattered light for enhanced contrast and sensitivity to transparent cells [24], vessel walls [25], and the inner segments of cone photoreceptors [26].

It has thus become clear that no single modality or technique exists that is optimized to visualize every potential cell or target in the functional retina. SLO and OCT each offer unique advantages: SLO permits detection of multiply scattered and fluorescent light while OCT provides high sensitivity, cellular-level depth sectioning, and phase-based approaches. In terms of clinical operability, due to its relatively small data size, real-time visualization of the AO-SLO

#462594 https://doi.org/10.1364/BOE.462594
Journal © 2022 Received 28 Apr 2022; revised 16 Sep 2022; accepted 20 Sep 2022; published 17 Oct 2022

Biomedical Optics EXPRESS

image stream is more computationally practical, whereas the large data size, dimensionality, and post-processing requirements hinder real-time visualization of the AO-OCT stream.

Multimodal AO (mAO) systems dating from the mid-2000s attempted to maximize functionality to visualize as many different retinal targets as possible, with varying degrees of additional complexity [27,28]. Imaging modes in early mAO systems operated independently or when simultaneously, with reduced performance necessary to match the imaging speeds of the different modes [29–32]. For example, AO-SLO devices typically use mechanically scanned beams that limit image acquisition to video rates (~15-60 Hz) and AO-OCT instruments were limited by swept sources or spectrometer detectors to hundreds of kHz A-scan rates. Combining these modes for simultaneous detection meant decreasing the OCT B-scan rate to the AO-SLO frame rate, leaving OCT volumetric imaging susceptible to eye motion artifact [29–32]. The invention of ultrahigh-speed imaging sources and full-field detectors heralded the potential of multimodal AO without compromise to the fundamental performance of the OCT channel. In particular, the development and commercialization of swept source Fourier-domain mode-locked (FDML) lasers enabled OCT line rates in the MHz domain, fast enough for video rate volumetric acquisition [33]. For example, by employing a 1.64 MHz FDML laser, Azimipour et al. demonstrated simultaneous AO SLO-OCT imaging of photoreceptors at an SLO frame rate of 6 Hz [34,35], which is compromised to match the OCT volume rate. Higher AO-OCT volume rates are possible only by sacrificing the pixel density (or field-of-view (FOV)) [36]. An alternative approach using line-scan OCT has been proposed to achieve multiple MHz A-line acquisition speeds for multimodal AO-OCT/SLO imaging [37]. While the results are impressive, due to the Gaussian nature of the illumination, the line-scan approach has a limited FOV of 1.4° and requires higher power illumination. Generally, imaging cellular structures using AO systems is often restricted to a small FOV imposed by the isoplanatic angle of the human eye, system aberration, and eye motion. With a few exceptions [38–40], most previously reported AO systems limited the imaging FOV to 2° or less, preventing wide adoption of AO into clinical practice. System complexity, imaging speed, and small FOV have thus limited the full development of multimodal AO approaches.

Concurrent with the improvements in imaging technology, the focus in ophthalmic imaging has shifted from static structural imaging to dynamic functional imaging. OCT angiography (OCTA) is a new, noninvasive technique that uses blood motion as a contrast mechanism to visualize retinal vessels and the effect that blood flow defects caused by ophthalmic and systemic vascular diseases have on retinal metabolism and health [41]. Intensity and phase-based functional techniques have been developed [35–37,42–47] and used to classify photoreceptors [36,37,44,45] and provide early indication of dysfunction [47]. RPE organelle motility has been proposed as a potential clinical biomarker of cell vitality [48]. Inner retina neuronal layer activation has also been imaged with full-field phase stable techniques [49]. These methods were typically demonstrated individually, and only rarely using multimodal systems, though some studies relied on the multimodal approach to directly enhance information of one channel using data from the other channel [36]. Given the complex neural pathways present in human visual processing in the retina, a more holistic acquisition approach may be garnered with multimodal and multifunctional retinal imaging.

In this study, we address limitations in the previous mAO approaches with the following aims: 1. To design and develop a system using new FDML swept source technology in which multiple imaging modes are combined without sacrificing the fundamental performance characteristics of each mode; and 2. To implement multifunctional imaging capabilities in a single mAO system, which could serve as a future platform to investigate the complex and multifaceted structure and function of the targeted retinal tissue. We integrated a 3.4 MHz FDML swept source laser into a simplified AO optical setup that employs two scanners for simultaneous AO-SLO and AO-OCT volumetric imaging at 13.4 Hz. We enriched the system with a stimulus port, wide-field operation

Biomedical Optics EXPRESS

for clinical applicability, and multiple operational modes comprised of acquisition protocols and post-processing software. The system achieves pan-macular and transretinal visualization of retinal cells and vessels, while also providing functional assessment of those same cells. The FDA FDML AO system will foster development and validation of a plethora of sensitive AO-based cellular structural and functional biomarkers for improved retinal disease diagnosis and treatment.

2. Methods

2.1. FDML AO system setup

The FDA FDML AO system achieves coextensive and synchronized multimodal retinal imaging using the same sample arm for AO-OCT and AO-SLO channels. As shown in the system schematic in Fig. 1, the sample arm consists of four pairs of reflective afocal telescopes that conjugate the pupil of the eye to the system's active components, including the Shack-Hartmann wavefront sensor (SHWS) lenslet array, the deformable mirror (DM, DM97-15, ALPAO, France), the vertical galvanometer scanner (GVS011, Thorlabs, Newton NJ USA), and the horizontal resonant scanner (SC-30, EOPC, New York NY USA). The telescopes are arranged in an out-of-plane configuration to compensate for system astigmatism [28,50] which arises from off-axis use of spherical mirrors (SM) and is known to degrade closed-loop AO performance. The optical layout and performance of the sample arm was designed and optimized in OpticStudio (Zemax LLC, Washington, USA). More details of the sample arm design are listed in Table S1 (Supplement 1). The system is designed to have a 7.4 mm collimated beam at the pupil and a maximum FOV of 4.5°×4.5° (1.35×1.35 mm^2) at the retina. The resonant scanner has a frequency of 3.348 kHz and operates in a bidirectional acquisition mode, yielding an effective B-scan frame rate / SLO line rate of 6.696 kHz.

Three near-infrared illumination sources are used for imaging: The AO-OCT imaging beam (λ_c = 1060 nm, $\Delta\lambda$=76 nm) produced with a 3.348 MHz FDML laser [33,51] (NG-FDML-1060-8B-FA, OptoRes GmbH, Munich, Germany); the AO-SLO imaging beam (λ_c = 786 nm, $\Delta\lambda$= 22 nm) produced with a superluminescent diode (SLD, EXS210060-01, Exalos, Schlieren Switzerland); and the AO beacon (λ_c = 850 nm, $\Delta\lambda$=35 nm) produced with another SLD (EXS210031-02, Exalos, Schlieren Switzerland). The front end optics setup including source integration, detection channel and SH design are described in Supplement 1. The AO-OCT and AO-SLO imaging beams are estimated to have transverse resolution of 2.89 µm and 2.16 µm for an eye with a 16.7 mm effective focal length, calculated using Rayleigh's criterion.

The system also includes an internal fixation channel, and a stimulus channel (see Supplement 1), which are combined and coaligned with the imaging beams in front of the eye using a dichroic beam splitter. The optical power of the AO-OCT, AO-SLO, and AO beacon beams measured at the cornea are limited to 1.6 mW, 200 µW and 50 µW, respectively. The maximum stimulus power is limited to 200 µW at 526 nm and 400 µW at 640 nm, and the pulse duration is limited to 5 ms. The total power at the cornea for all operational modes is below the ANSI standard Z80.36 classification for Group 1 ophthalmic instruments [52].

Custom system control software was developed in LabVIEW (National Instruments, Austin TX) for system synchronization and control, and real-time visualization and flexible data saving (Supplement 1). The AO-SLO frame and AO-OCT B-scan are displayed in real-time to permit visual validation of AO image quality and determination of system focus for imaging cells at different depths. The flexible saving scheme allows collection of data from either or both of imaging channels (AO-SLO and AO-OCT).

2.2. System assessment methodology

System optical resolution was evaluated in OpticStudio in comparison to the diffraction limit using a paraxial model eye. Beam displacement was also predicted in OpticStudio at the DM and

Biomedical Optics EXPRESS

eye pupil planes. Sensitivity roll-off was determined by moving the reference arm while a plano mirror was placed in the sample arm following a previously reported method [53]. AO-OCT A-scan profiles of the plano mirror were averaged for the system axial resolution measurement.

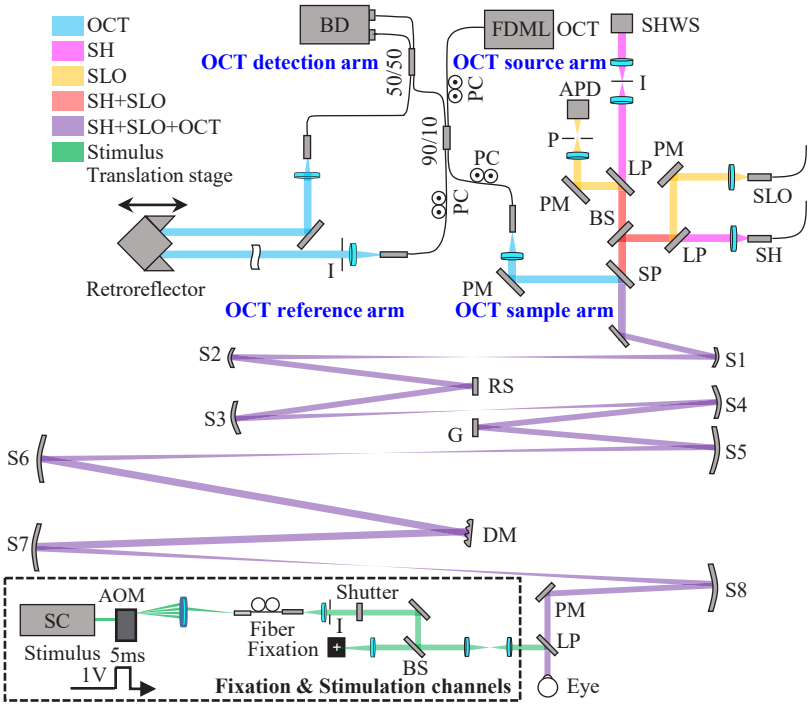

Fig. 1. Schematic layout of the FDA FDML AO system for multimodal and multifunctional retinal imaging flattened for clarity. The swept source OCT uses a typical Mach–Zehnder interferometer design which consists of the source, sample, reference, and detection arms. The OCT reference arm consists of a group of plano mirrors and a retroreflector to match the double-pass optical path length (OPL) of the sample arm. **Key:** AOM: acousto-optic modulator; APD: avalanche photodiode; BD: balanced detector; BS: beam splitter; DM: deformable mirror; G: galvanometer; I: iris; LP: long-pass dichroic filter; P: pinhole; PC: polarization controller; PM: plano mirror; RS: resonant scanner; S: spherical mirror; SHWS: Shack-Hartmann wavefront sensor; SP: short-pass dichroic filter; SC: supercontinuum.

2.3. Participants and imaging

AO-SLO images and AO-OCT volumes with various FOVs were simultaneously taken from two healthy subjects (S1: 37 yrs and S2: 27 yrs) with no known retinal pathologies for multimodal and multifunctional imaging following the designed imaging protocols listed in Table S2 (Supplement 1). The protocols aimed to demonstrate the system capabilities to extract different structural and functional information across the entire retinal depth, the wide field design for clinical usability, cellular-level performance, and angiography for vasculature visualization. For all structural and functional imaging (Protocols 1-4), data were acquired at an OCT volume/SLO frame rate of 13.4 Hz. Images were registered and averaged in three dimensions (3D) with sub-cellular level accuracy [16] to demonstrate inner retina, photoreceptor, and RPE cell structural imaging (Protocols 1-3). For cone functional imaging (Protocol 4), at volume 5 of 15, a 5-ms pulse of visible light (526 nm or 640 nm) was delivered to the retina. It is estimated to bleach 21.3% and 9.9% of the photopigments with the 526 nm and 640 nm stimuli respectively [54]. Eight

Biomedical Optics EXPRESS

videos (which each contain 15 OCT volumes) were collected and averaged for each stimulus condition for improved signal-to-noise ratio (SNR). The subject was instructed to close their eyes for 90 s between successive video acquisitions to record evoked photoreceptor response absent artifact from the preceding visible stimuli [44]. After the 90 s dark adaptation, the unbleached photopigments reach 95.2% and 98% for 526 nm and 640 nm stimuli respectively [54]. The phase difference between cone inner segment/outer segment junction (IS/OS) and cone outer segment tip (COST) was extracted and converted to optical path length change (ΔOPL) for cone functional assessment, following a previously reported method [42,43]. Eight repeated (4 forward and 4 backward) AO-OCT B-scans were collected at each slow scan position for OCT angiography imaging (Protocol 5) at a volume rate of 1.675 Hz. During imaging acquisition, system focus was set at the layer of interest to maximize the sharpness of the imaged structures. A speckle variance (SV) method [55] was implemented to visualize retinal and choroidal vessels.

3. Results

3.1. System performance

Figure 2(A) shows the ray trace predicted spot diagram of the FDA FDML AO system at the retina with SH wavelength (850 nm) for scan angles over the 4.5°×4.5° FOV without AO correction. All rays fall inside the solid circle denoting the diffraction-limited blur size. The maximum wavefront root-mean-square (RMS) error measured across the entire FOV was λ/32, more than two times smaller than the diffraction-limited criteria (λ/14). Figure 2(B) shows the beam displacement at two pupil conjugate planes with nine scanning positions depicted as colored dots. The beam displacement ranges for three FOVs are 40 μm, 100 μm and 220 μm at the DM plane, and 15 μm, 40 μm and 105 μm at the eye pupil plane, which are at least three times smaller than the projected SH pitch size (220 μm at DM; 342 μm at the eye). As shown in Fig. 2(C), the measured system axial resolution is 11.6 μm in air which corresponds to 8.4 μm in the eye ($n = 1.38$). The measured system sensitivity is -82.9 ± 1.0 dB, and the measured sensitivity roll-off is ~6 dB over the first ~2 mm and ~10 dB over the first 3.5 mm from zero pathlength (Fig. 2(D)).

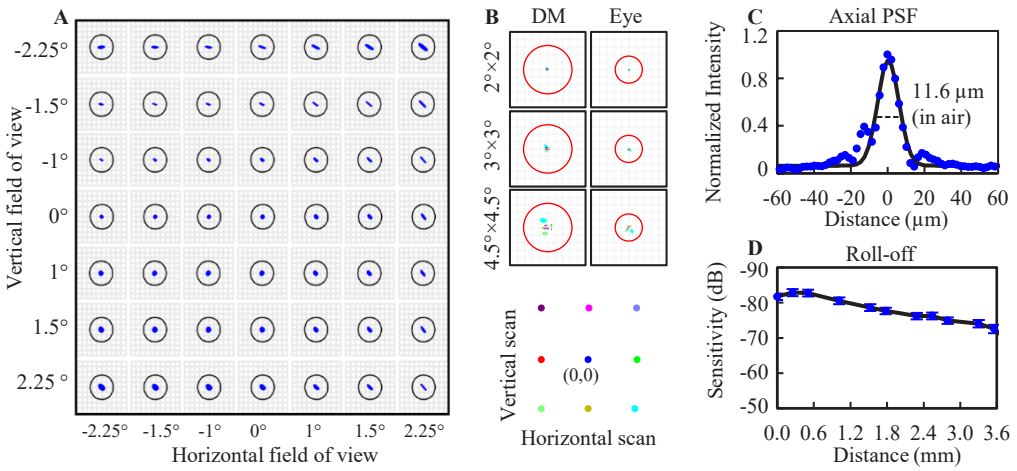

Fig. 2. Performance of the FDA FDML AO system. **A.** Ray trace predicted image quality as a function of scan angle with a model eye. Solid black circles denote diffraction-limited blur size. **B.** Ray trace predicted beam displacement at two pupil conjugate planes. Red circles denote projected SH lenslet size. **C.** OCT axial resolution (see Data File 1 [56]). **D.** OCT sensitivity roll-off (see Data File 2 [57]).

Biomedical Optics EXPRESS

3.2. Multimodal structural imaging

The FDA FDML AO system was designed with a multimodal setup to simultaneously provide multiple real-time visualizations (AO-SLO frame and AO-OCT B-scan) with which to investigate retinal cells. The real-time visualization ensures the retinal cells of interest are within optimal focus for either modality. An example is shown in Fig. 3 and Visualization 1 with cells at different retinal depths imaged simultaneously by the AO-SLO and AO-OCT channels. Overall, the images from both channels show similar retinal structures with precise system focus control (Fig. 3(B)), while also exhibit subtle distinctions which could be the results of speckle differences, a small focus shift between channels, OCT slab selection, or fundamental disparity between the detectors. For example, the AO-OCT *en face* images of the inner retina appear more speckled; and the cone photoreceptors in the AO-OCT channel are more uniform in appearance and can be seen below large retinal blood vessels in comparison to the cells in the AO-SLO channel.

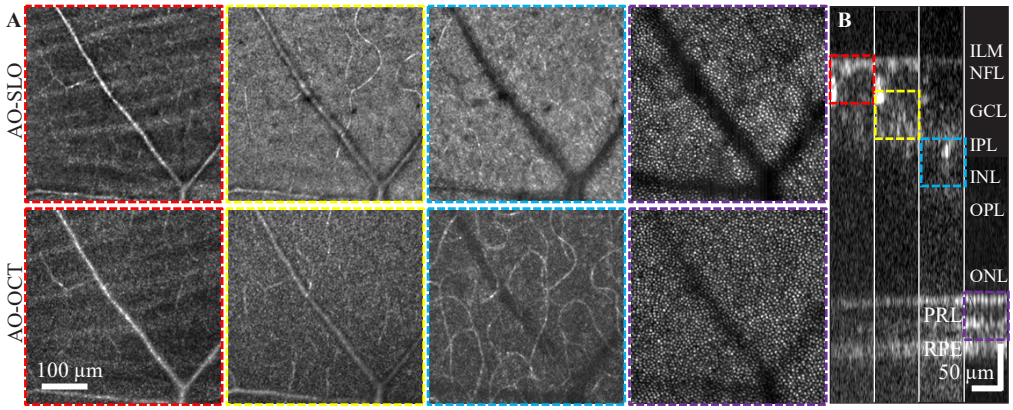

Fig. 3. Co-registered averaged 1.5° FOV simultaneous AO-SLO (**A** top) and AO-OCT (**A** bottom) retinal images from S1 with the system focus set approximately at four depths (ILM-GCL; GCL-IPL; IPL-OPL and PRL) which are determined by the local intensity of the AO-OCT B scans and AO-SLO real-time visualizations. The AO-SLO data were collected with a one Airy disk diameter (ADD) pinhole. The AO-OCT *en face* images were created by the amplitude projection of a AO-OCT 50 µm slab through the system depth of focus (DOF) [8]. Each image was averaged across 15 datasets and was produced from videos in Visualization 1. B shows the average of 15 AO-OCT B-scans along the slow scan direction, the image are stitched from four sub-images that were acquired with system focus at the four primary depths from the same retinal location. The color-coded dash boxes represent the ranges for generating the corresponding AO-OCT *en face* images in **A**.

The FDML AO-OCT sub-system offers ultrahigh acquisition rates, exquisite sensitivity, and 3D cellular resolution which together allow resolution of detailed retinal features in both inner and outer retina layers. Figure 4 shows AO-OCT data obtained at 10° temporal retina from subject S1 with system focus set at the inner retina. 300 volumes from 20 videos acquired across 15 min with average time interval of 0.5 min were registered and averaged. A time-lapse video was created for tracking the movement of macrophage processes (Visualization 2). AO-OCT volumetric and B-scan perspectives are shown in Fig. 4(A)-(B). Depth-resolved *en face* projections reveal retinal macrophage cell bodies and their processes [17] just above the inner limiting membrane (ILM, Fig. 4(C)), fiber bundles and individual axons from ganglion cells in the nerve fiber layer (NFL, Fig. 4(D)), and a mixture of midget and parasol ganglion cells in the ganglion cell layer (GCL, Fig. 4(E)). While macrophage processes were in constant motion, most of the cell bodies remained relatively immobile over the short durations of the time-lapse video (Visualization 2). GCL somas at the imaged location have a density of 4698 cells/mm^2 and an averaged cell diameter

Biomedical Optics EXPRESS

of 12.95 ± 2.26 µm, measured using a weakly-supervised deep learning algorithm for automated GCL soma segmentation [58], which are in agreement with the previously reported results on healthy subjects at a similar location obtained with ~800 nm imaging light [16,59]. Despite the much shorter exposure time for single A-scan acquisition (0.3 µs) and longer wavelength (1060 nm) compared with the fastest spectral domain-based AO-OCT system (2 µs exposure time and 785 nm wavelength) reported for imaging GCL somas [16], the results shown in Fig. 4 suggest that our system has sufficient sensitivity to resolve weakly reflective cells like GCL somas with a similar amount of volume averaging but with 6.7× faster acquisition speed.

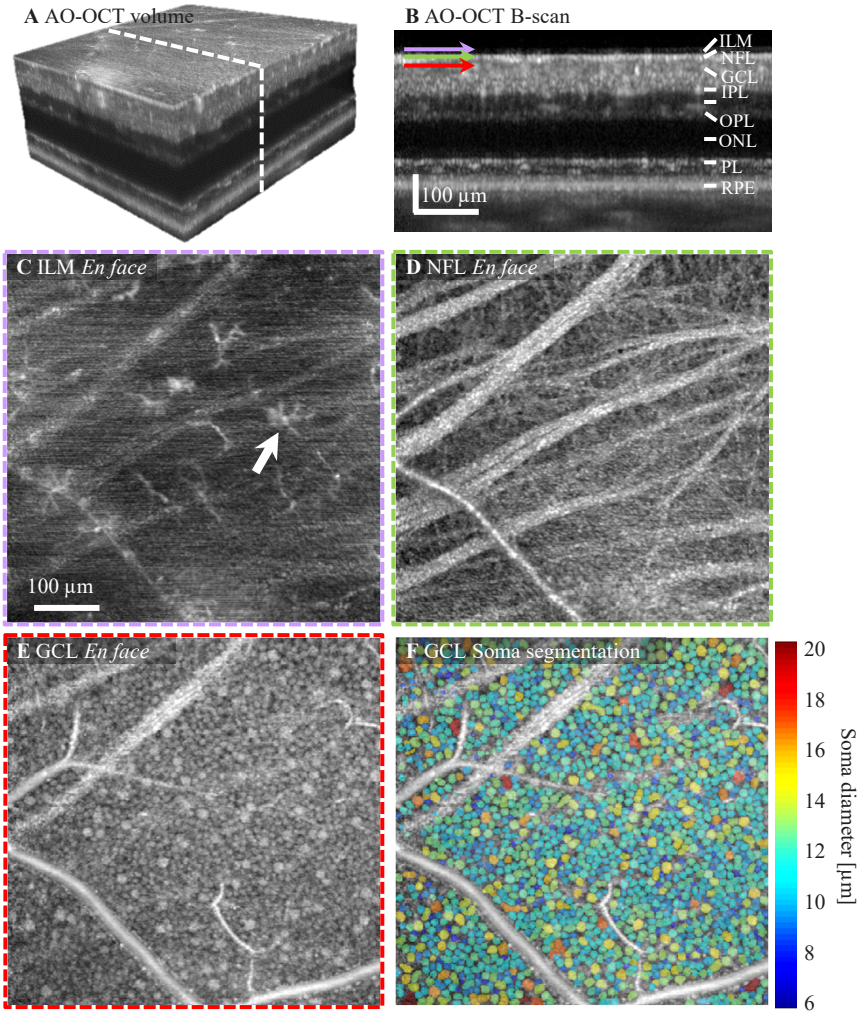

Fig. 4. Structural images of inner retinal cells collected at 10° temporal to the fovea from subject S1 with an average of 285 AO-OCT volumes. **A.** Isometric view of registered and averaged AO-OCT volume with white dashed line denoting cross-section of retina shown in **B**. Images shown in **C-E** were extracted at depths of the ILM, NFL, and GCL, respectively. **C.** Retinal macrophages (both cell body and processes) shown at the surface of the ILM. **D.** Bundles and individual ganglion cell axons disperse across the NFL. **E.** A mosaic of GCL somas of varying size tile the layer. **F.** GCL soma 3D segmentation. The false color map shows the segmented GCL somas that are color coded with cell diameter.

Biomedical Optics EXPRESS

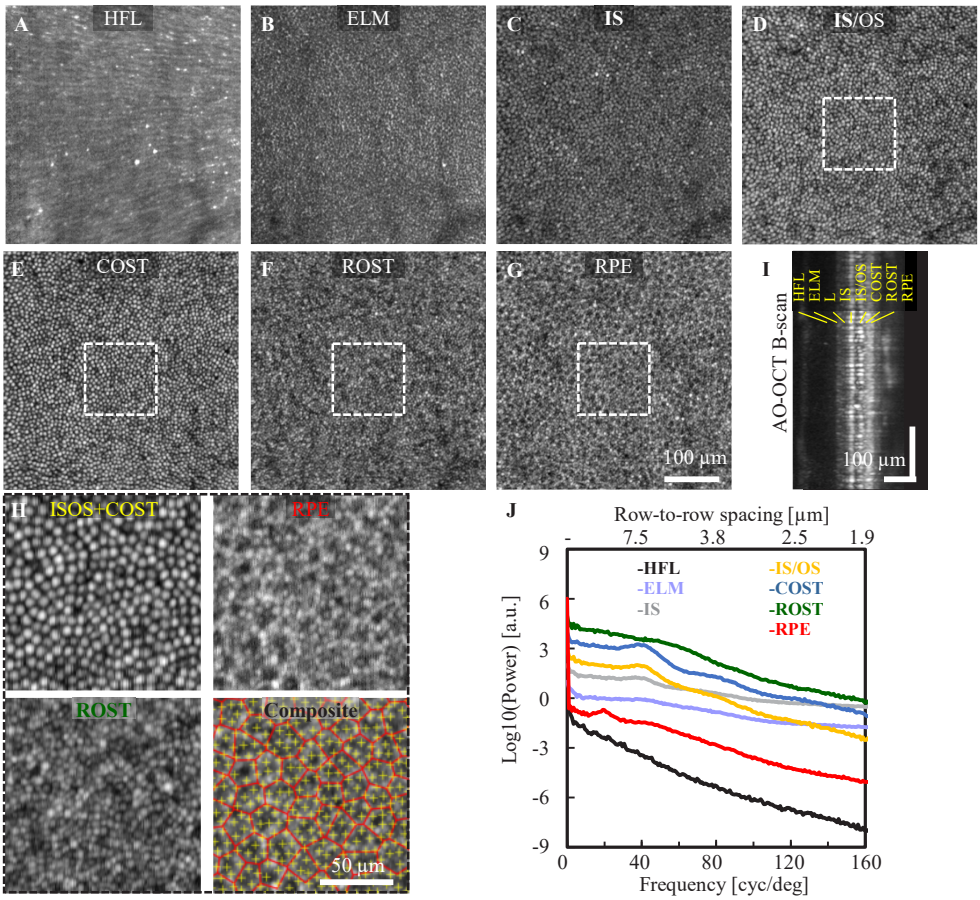

Fig. 5. Structural images of outer retinal cells collected at 3° temporal to the fovea from subject S2 with an average of 190 AO-OCT volumes. *En face* views of outer retinal cells at different depths show different spatial content. **A.** The HFL shows radial striation pattern of Henle fiber bundles, **B.** ELM intensity show negative correlation with underlying cone photoreceptors in (C-E), **C**. Photoreceptor IS, **D.** Photoreceptor IS/OS junction. **E.** COST, **F.** ROST layer exhibits a hyper reflective mosaic with higher spatial content, presumably from individual rods, **G.** RPE, **H.** Magnified views at the cone (IS/OS + COST), rod, and RPE layers (white boxes in **D**-**G**) along with the composite view that shows the marked cell locations (yellow cross: cone and red Voronoi: RPE). **I.** An average AO-OCT B-scan of outer retina with labeled axial depths, and **J.** Power spectral analysis at the corresponding axial depths (see Data File 3 [60]). For visualization purposes, spectra are normalized to the same DC level and displaced vertically by retinal layers. Images are showed in logarithmic scale.

Biomedical Optics EXPRESS

Cellular details were also resolved with the system focus set to the outer retina at the photoreceptor-RPE complex (Protocol 2). A total of 10 videos (19 volumes/video) were acquired at 3° temporal retina from S2 with 1.5 minute video separation to allow RPE organelle motility for RPE imaging [13,48]. The AO-OCT images reveal: a radial pattern of Henle fibers at the Henle fiber layer (HFL) (Fig. 5(A)); the mottled reflections surrounding cones at the external limiting membrane (ELM) (Fig. 5(B)) resulting in a negative correspondence in reflectance with the cones (Fig. 5(C)-(E)) at IS, IS/OS and COST; high spatial frequency content with smaller features, presumably individual rod photoreceptors, at the rod outer segment tip (ROST) layer (Fig. 5(F)); and the hexagonal arranged retinal pigment epithelial (RPE) cell mosaic at the RPE layer (Fig. 5 G). The distinct separation between outer retina layers in the averaged B-scan view (Fig. 5(I)) also demonstrates the system's axial sectioning capability for distinguishing cells/features in the outer retina. According to Rayleigh's criterion, the theoretical transverse resolution is predicted to be 2.89 μm (AO-OCT), which is the approximate width of a rod photoreceptor. Our ability to resolve a higher spatial content at the ROST layer compared to the cone and RPE layers (Fig. 5 H) indicates the gain in confocality afforded by the OCT channel, resulting in a system confocal resolution of 2.1 μm. The power spectral analysis shows a 7.04 μm and 14.3 μm row-to-row spacing for cone photoreceptor and RPE cells, respectively. Very intriguingly, the power spectrum shows a peak at the same spatial frequency for ELM, IS, IS/OS and cone outer segment tip (COST), and elevated energy is evident for ROST, indicating the dominant signal from ELM to COST is from cones and rods at the ROST, though, counting individual rods is challenging at the current eccentricity and pixel sampling (0.9 μm/pixel). Changing the imaging location to the rod dominant region in the periphery and increasing the pixel density could potentially improve rod visibility, which remains for future investigation.

3.3. Multimodal wide field imaging

Due to imaging system aberrations, eye motion, and the isoplanatic patch of the human eye, previous AO systems often limit the imaging FOV to <2°, imposing a challenge for AO clinical translation. Here, we address the first two factors with an optical system designed to minimize system off-axis aberrations and an ultra-high speed FDML-based approach (~3.4 MHz A-scan acquisition rate) to mitigate eye motion artifact to achieve an imaging field of 4.5° for cellular imaging (Protocol 3). We performed initial visualization of the overall distribution of nerve fiber bundles (NFB) and ILM macrophages with wide field scans, as shown in Fig. 6. With proper axial layer segmentation, NFB and retinal macrophages are delineated with high definition in a wide region spanning ~30° across the macula, achieved by montaging seven AO-OCT videos collected in only a few seconds. These preliminary data show the clinical feasibility of our approach for structural characterization of retinal NFBs and macrophages for ocular and neurological diseases such as glaucoma [59] and multiple sclerosis [61].

The wide-field imaging feature may also be beneficial for rapid assessment of the structural health of smaller cells, like cone photoreceptors. Figure 7 shows averaged AO-SLO images taken across a similar eccentricity range as Fig. 6 with eleven overlapping 3°×3° AO-SLO scans. The 3° scans provide a reasonable trade-off among total imaging area (~30° macular strip), imaging time (~10 min total acquisition time), and digital sampling densities (~0.57 pixels/μm). Fig. S1 (Supplement 1) has further examples across a range of pixel densities. The wide-field scans permit visualization of cones across the entire macula. Near the fovea (<1° to the fovea), the 3° field image did not have sufficient spatial pixel sampling to resolve individual cones. However further reducing the field size to 0.75° with a corresponding increase in density to ~2.3 pixel/μm allows better delineation of the cones at the fovea (Fig. S2, Supplement 1). The wide field images show the cone density decreases from approximately 36,000 cells/mm^2 at 1° to 8,400 cells/mm^2 at 8° (Fig. S3 in Supplement 1, cone density is provided in Data File 4 [62]), within the range reported previously [63]. Cones above 8° locations are difficult to count from our images due

Biomedical Optics EXPRESS

to their multimodal behavior [64] and the mixed signals from adjacent rods, and more robust AO-SLO cone density measurement in the peripheral retina likely requires implementation of split detection methodology [26], which can be further exploited for views of dysfunctional cones. Implementation of the split detection approach remains for future investigation.

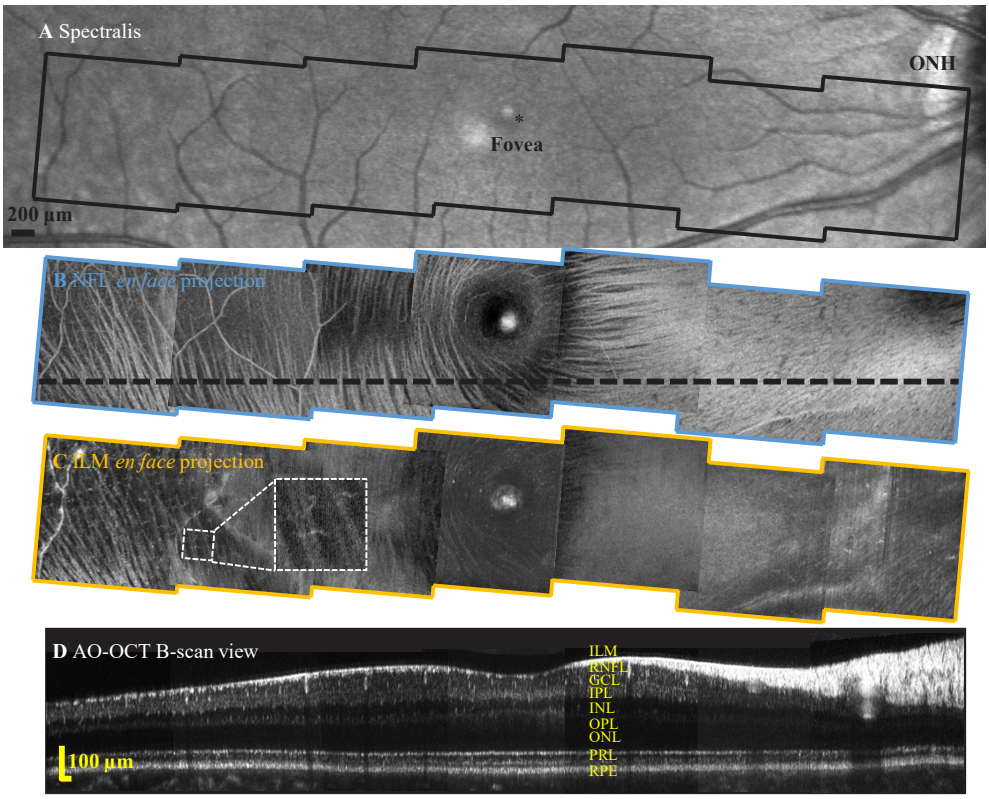

Fig. 6. Representative wide-field inner retina images from subject S1 collected with the FDA FDML AO system. **A.** Spectralis macular scan. *En face* projection views over a -14° to 14° eccentricity range from seven 4.5°×4.5° FOV AO-OCT scans of **B**. NFBs at NFL and **C.** macrophages just above the ILM. Inset shows magnified view of one representative macrophage cell at 8° eccentricity. **D**. AO-OCT B-scan view corresponds to the black dashed line in **B**.

3.4. Multifunctional imaging

Phase-sensitive AO-OCT (PhS-AO-OCT) is a technique that quantifies photoreceptor function via phase changes in back-reflected light, providing a direct assessment of individual cone function, and therefore holds promise to provide functional disease biomarkers for applications beyond vision science [35,43–45,47]. Here, we implemented a phase-sensitive AO-OCT approach coupled with the stimulus channel in our FDML AO system to measure cone function (Table S2, Protocol 4. Supplement 1). A representative AO-OCT B-scan (Fig. 8(A)) shows clear separation between cone IS/OS, COST, and retinal pigmental epithelium (RPE). The AO-OCT *en face* projection from the IS/OS junction to the COST (Fig. 8(B)) shows individual cone photoreceptors resolved across the entire 1.5°×1.5° FOV. After visual stimulus, the OCT signal showed increased OS optical path length (Fig. 8(D)) which is expected to return to baseline shortly thereafter (in tens of seconds). The averaged phase change between IS/OS and COST

Biomedical Optics EXPRESS

layer was 1.7 rad, corresponding to 142 nm (Fig. 8(F)). The cone responses to two visible stimuli (526 nm and 640 nm) result in three distinct clusters in the principal component space following a previously reported analysis method [44]. The three clusters represent L-, M-, and S- cones, and their corresponding phase changes to 640 nm visible light are shown in Fig. 8(F), where the overall phase change for all cones is shown as a black curve. The trichromatic cone mosaic is shown in Fig. 8(G). As expected, the L-cones have the strongest response, M-cones have a moderate response, and S-cones have the weakest response to 640-nm stimulus, agreeing with their expected spectral sensitivity. The stimulus experiment results demonstrate the system capability for measuring cone function, leading to new functional biomarkers for detection of early outer retina diseases, such as age-related macular degeneration (AMD).

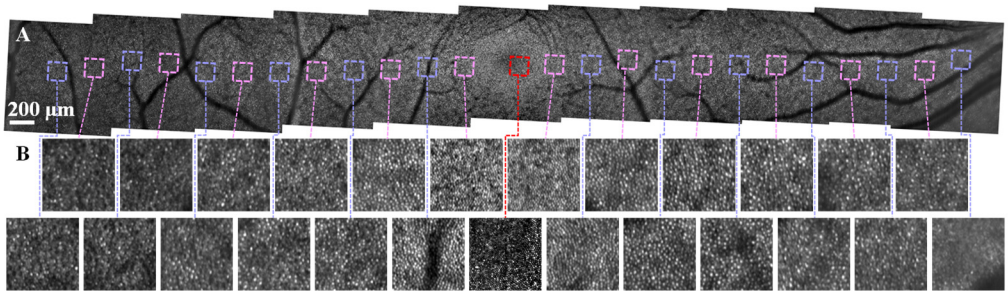

Fig. 7. Representative wide-field retinal cone images from subject S1 collected with the AO-SLO channel of the FDA FDML AO system. **A.** Montage of eleven AO-SLO scans with a 3°×3° FOV across a -14° to 14° eccentricity range. **B.** Enlarged views of the cone mosaics at the corresponding nasal and temporal locations labeled at square boxes in **A**. Each sub-region is a 150 μm×150 μm field. The sub-region at the fovea was acquired with a 0.75°×0.75° FOV scan (Fig. S2 in Supplement 1) with increased digital sampling.

3.5. AO-OCTA imaging

The OCT angiography (OCTA) approach has provided clinically relevant information about inner retinal vessels and vascular disorders for ocular diseases such as diabetic retinopathy and AMD [66]. However, reliable characterization of retinal capillary morphology using clinical OCTA systems remains challenging due to their limited transverse resolution. Increased acquisition speed to the MHz range has yielded higher contrast images of retinal vasculature [67,68]. Despite its success in clinical OCT devices, OCTA methodology has not been widely implemented in existing AO-OCT systems. Only a few studies reported imaging retinal vessels [69] and choriocapillaris [20], all with relatively small FOVs and intensive averaging. We modified our scanning protocol to allow eight repeated scans (4 forward and 4 backward) per slow scan position for AO-OCTA imaging over a 5°×5° field by montaging the four volumes around the fovea (Table S2 in Supplement 1, Protocol 5). Due to the reduced depth-of-focus under a large pupil condition, the system focus was placed approximately at the middle of the inner retina and just below the photoreceptor-RPE complex to enhance visualization of capillaries and vessels in the three retinal plexuses and the choriocapillaris (CC) respectively. Vessels at three depths (retinal vessels, CC, and choroid) were segmented separately from these scans. Considering the non-linear temporal separations of the A-scans in adjacent B-scans acquired with bi-directional scanning, we applied a SV analysis method [55] to the forward and backward scans independently, then averaged the OCTA volume from forward and backward scans to produce the final AO-OCTA volume. The corresponding OCT intensity volume was also produced by directly averaging the eight B-scans that were acquired at the same slow scan position.

Biomedical Optics EXPRESS

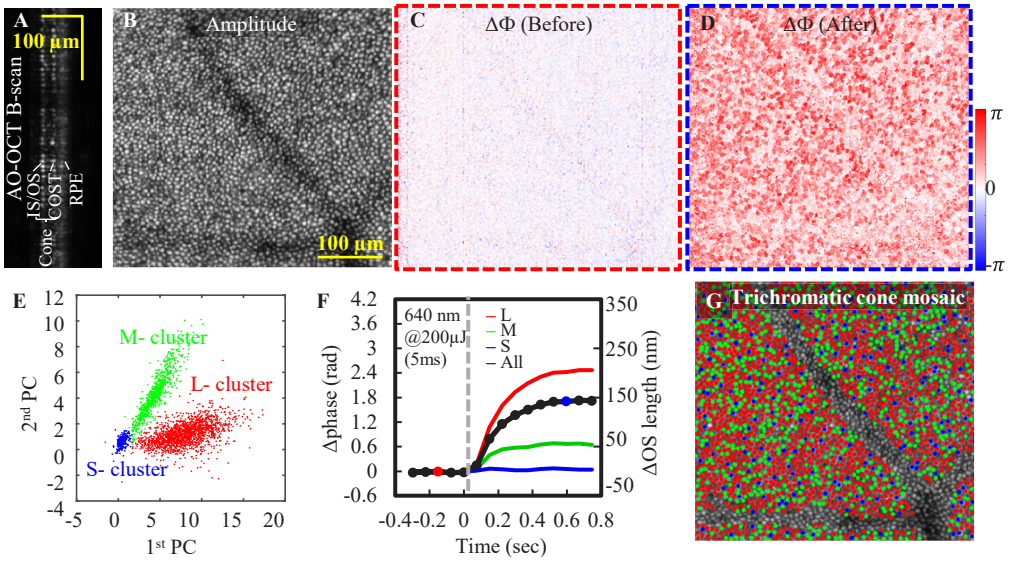

Fig. 8. Cone structural and functional characterization in subject S1 at 3° nasal retina. **A.** B-scan and **B.** *en face* views show reflectance of individual cones. Cone ΔOPL between IS/OS and COST in response to 640-nm stimulus at time points 3 in **C.** and 13 in **D**. **E.** Plot of first two principal components (PC) used to classify cone types. **F.** Shows the averaged cone response at all time sequence (see Data File 5 [65]). Averaged cone response in **C.** and **D.** are shown as the red and blue filled circles. The classified averaged response for L-, M-, and S- cones are denoted as red, green and blue curves. **G.** Map of the trichromatic cone mosaic.

As shown in Fig. 9, signals that arise from vessels are enhanced in AO-OCTA volumes, which is evident from both B-scan (Fig. 9(A)-(B)) and *en face* views (Fig. 9(E)-(G)). The CC is clearly delineated with AO-OCTA volume (Fig. 9(F)), and no similar structure is revealed in the AO-OCT intensity image (Fig. S4B in Supplement 1). A 16-µm separation between RPE and CC was found by comparing the A-scan profiles of AO-OCT and AO-OCTA data, which is consistent with the previously reported range [20]. The cusp in the power spectrum (Fig. 9(H)) corresponds to a fundamental spacing of 39.5 µm; that is, the average spacing between adjacent CC segments, which agrees with the previous result [20]. Visually, the retinal vessels in the AO-OCTA volume also have higher contrast than the AO-OCT volume (Fig. S4 in Supplement 1), which can be also revealed with high contrast using the AO-SLO intensity variation method (Fig. S4D). The deeper choroidal vessels have similar appearance between the two volumes, but the increased penetration from the longer FDML wavelength (1060 nm) is evident in the visualization of these deeper vessels. In conclusion, the system generates promising results for resolving capillaries at their densest location in the human body using an AO-OCTA modality with a relatively large scan size, and provides an additional capability for assessing vasculature integrity. We also note that our FDML AO-OCTA volumes were acquired in less than a second (0.6 s), permitting rapid montaging of vessel images over a large retinal region (Fig. 10). This modality also offers the opportunity to explore the relationship between the cone-RPE-CC complex (Fig. 10), providing yet another powerful tool to study AMD.

Biomedical Optics EXPRESS

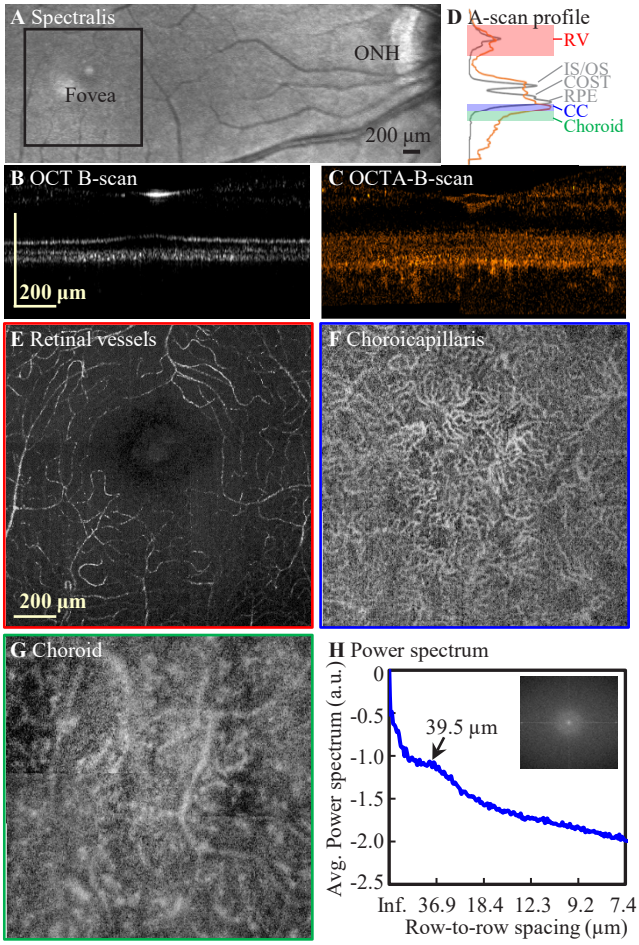

Fig. 9. Representative AO-OCTA images collected at the fovea from subject S1 with four 3°×3° FOV scans. **A.** Spectralis SLO scan. B-scan cross sectional views of **B.** AO-OCT and **C.** AO-OCTA and their corresponding A-scan profiles in **D** for OCT (gray) and OCTA (orange). AO-OCTA *en face* projections at the depth of **E.** retinal vessels (RV) (red), **F.** choriocapillaris (blue), and **G.** choroid (green). The depths of the integrated projections are defined by the color-shaded regions in **D. H.** Power spectral analysis of **F.** shows a peak at the cross-correlation fundamental frequency (see Data File 6 [70]).

Biomedical Optics EXPRESS

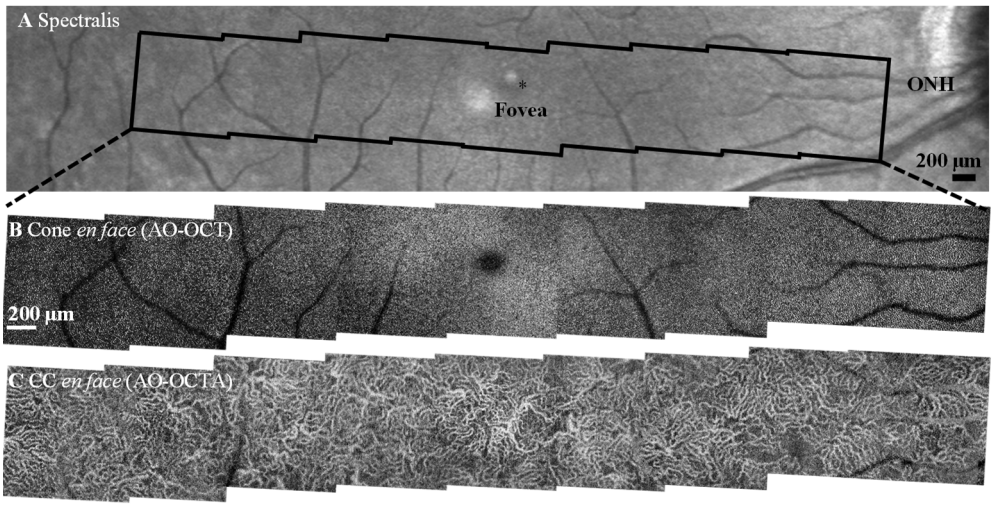

Fig. 10. Representative wide-field images of outer retinal features from subject S1 collected with the FDA FDML AO system. **A**. Spectralis macular scan. *En face* projection views over -11° to 11° eccentricity range from nine 3°×3° FOV scans. **B.** AO-OCT intensity projection (IS/OS to COST) shows better delineation of the cone photoreceptor mosaic compared to AO-SLO montage from the same region (Fig. 7) due to the exclusion of signals from neighboring rod photoreceptors and underlying RPE cells. **C.** Corresponding AO-OCTA scans of the choriocapillaris.

4. Discussion and conclusion

Herein we present the optical design, performance, and initial human subject imaging of the FDA FDML AO ophthalmic imaging system. The FDML AO system, with features of high speed, dense sampling, large FOV, real-time visualization, and flexible acquisition and data collection, is a powerful tool to effectively study different retinal cells and their function. The unique multifunctional and multimodal system design, in conjunction with exquisite system sensitivity and 3D resolution, enable microscopic imaging of various retinal cells (GCL somas and macrophages in Fig. 4; photoreceptor and RPE cells in Fig. 5), vasculature (AO-OCTA imaging in Fig. 9 and Fig. 10), and other structures across the entire retina, as well as providing photoreceptor function assessment with optoretinography (Fig. 8). The ultra-high speed acquisition and out-of-plane optical design permit rapid scans with relatively large FOV while maintaining optimal AO correction (Figs. 6, 7, 9, 10, and S1).

The FDA FDML AO system was designed to overcome issues that limited performance in previous multimodal designs [29–32,34,71]. Early attempts to combine SLO with Fourier-domain OCT limited OCT B-scan rates to the SLO frame rate, resulting in extremely low OCT volume (C-scan) rates. This left OCT volumetric imaging susceptible to eye motion artifact and led to long, difficult imaging sessions in order to collect full volumetric structural information [29–32]. With a time-domain OCT approach, Felberer et al. [71] achieved co-extensive scanning, but the approach was limited to visualization of one layer of interest at a time and required precise, high-speed axial motion correction, adding to system complexity. The recent advances in the development of ultrahigh-speed swept sources [33] enabled an OCT volume rate that matched the SLO frame rate. However, the earlier integration of a 1.64 MHz swept source into a multimodal system degraded the capability of the SLO channel – in this case a slow (sub-10 Hz) SLO frame rate [34] or compromised spatial sampling and FOV for the tradeoff of a faster SLO frame rate [36]. Though a very high effective A-line speed was demonstrated with a line scanning OCT

Biomedical Optics EXPRESS

approach in a multimodal AO SLO/OCT system, the Gaussian beam illumination fundamentally constrained the size of the imaging field (<2°) and required relatively high input power sources for imaging [37]. These limitations (slow acquisition speed, small imaging field, extra system complexity) prevented broad adoption of mAO devices into clinical practice. In addition, the capability of pan-macular and transretinal visualization of retinal cells and structures has yet to be fully utilized for clinical investigations.

Our multimodal AO technology was designed to address the gaps in previous mAO implementations to achieve multimodal and multifunctional cellular imaging and also a relatively large FOV for clinical use. To achieve this, we combined several recent technological advances: a 3.4 MHz FDML swept source for ultra-high speed OCT acquisition while achieving high sensitivity and low roll-off; an out-of-plane optical design to minimize system off-axis astigmatism; a simplified optical design with only two scanning elements; pixel-level registration and integrated data analysis to allow cellular-level imaging performance; electronic design for simultaneous acquisition, flexible data collection, and real-time display of acquired images. The FDA FDML AO system was also designed to help overcome the challenge of AO clinical translation, which is primarily expressed in terms of the small FOVs and time-consuming montaging necessary to get a global view of ocular health [28]. This challenge is ultimately one of a practical matter – how to achieve sufficient pixel density for cellular imaging across a wide field spanning tens of degrees. And this challenge can only really be solved with higher speed imaging. But it is also a matter of 'smart design', where the system and method are matched to the retinal cell or target of interest. So, for example, ILM macrophage distribution can be quantified with the wide-field scan shown in Fig. 6(C), but a measure of function (i.e., process motility) may require a higher pixel density (to resolve processes) and smart temporal sampling (to capture the motion on the correct timescale) [17]. In the FDA FDML AO system, we have demonstrated excellent optical performance up to a 4.5° field size (Fig. 6). Recent full-field OCT systems have demonstrated even higher volume rates [49,72], giving confidence that small fields do not remain one of the inherent limitations of AO technology. The other challenge to AO clinical translation has to do with a balance of complexity and functionality: our system realizes technological gains that lead to a reduction in complexity while adding features that have been demonstrated in other AO systems that are becoming essential for probing retinal tissue. Finally, the FDA FDML AO system design includes a transition to more functional measures, including photoreceptor function via stimulus evoked optical path length elongation in the photoreceptor outer segment that can be resolved by Ph-AO-OCT, and AO-OCTA to probe the important contribution of blood flow to the overall metabolic health of the eye. Indeed, these functional measures can easily be combined in a future investigation to simultaneously detect correlations between photoreceptor and RPE dysfunction and deficits in flow in nearby individual choriocapillaris segments. Neurovascular coupling can only be properly examined with multiple perspectives and measures of the neurovascular unit.

There were several challenges and limitations in the various multimodal and multifunctional implementations in the FDA FDML AO system. One limitation is inherited from the use of an FDML laser. The FDML laser increases the A-line acquisition rate by optical buffering to create successive time-delayed copies of the original sweep using long optical spools [33,51]. The imperfections in the splitting ratio of the fiber couplers in the buffering stage cause noticeable amplitude differences among the buffer sweeps (Fig. 2(D)). The spectral mismatch in the interference signal leads to phase distortion in the A-lines originating from different buffers. This buffer-caused phase difference may decrease the SNR of the OCTA images (Figs. 9 and 10) and the system sensitivity to measure the light induced phase changes of the cones (Fig. 8). A numerical spectral resampling algorithm has demonstrated significant improvement in phase alignment among the buffers [73]. The implementation of the phase correction approach will be explored during future system optimization. In addition, the system acquires data at a rate (4 GS/s) that challenges even the fastest personal computers. This limits the overall duration of acquired

Biomedical Optics EXPRESS

data to only a few seconds and can have implications when longer durations are required to capture, for example, the full course of stimulus-evoked photoreceptor response or RPE motility time constant, both of which require 5-10 second acquisition durations [48]. We have overcome this partially by implementing OCT volume sampling at a lower rate but with a longer duration (not demonstrated in this paper). Furthermore, the bidirectional scan required implementation of an OCTA algorithm that separately processed the forward and backwards scans. The high B-scan acquisition rate also requires consideration in terms of the optimal OCTA B-scan interval for high-contrast retinal capillary visualization [74]. Lastly, the longitudinal chromatic aberration of the human eye can result in focus offset between the AO-SLO and AO-OCT images. The chromatic focus difference is corrected in our system by shifting the achromatic lenses used for beam collimation at the back end of the system until the sharpest photoreceptor images were achieved on both channels with AO correction. Alternate approaches for longitudinal chromatic aberration compensation that may be implemented in future optimization include use of an achromatizing lens or Badal system, which require either a customized design [75] or an increase in system complexity. The overall advantages of ultrahigh-speed imaging in the MHz range far exceed these various challenges, which can be overcome with smart configurations and post-processing algorithms.

The FDA FDML AO system achieves higher acquisition speed, lower depth roll-off, and comparable sensitivity and 3D resolution as previous mAO systems in clinical use [17,32,59,61]. We expect the FDA FDML AO system will prove to be a powerful platform with which to investigate a host of ophthalmic and neurological diseases in future investigations, including age-related macular degeneration, diabetic retinopathy, retinitis pigmentosa, multiple sclerosis, and Alzheimer's disease. The integrated features and our initial promising results demonstrate capabilities that can be applied to basic science research for investigation of retina physiology through structural and functional assessment, but also to establish AO as an effective tool and clinical endpoint for diagnosis and treatment of retinal diseases.

Funding. Food and Drug Administration (FDA) of the U.S. Department of Health and Human Services (HHS) (Critical Path program).

Acknowledgments. We thank Donald Miller (Indiana University School of Optometry) for use of OCT 3-D registration software. We thank Achyut Raghavendra (FDA) for technical assistance.

Disclosures. The mention of commercial products, their sources, or their use in connection with material reported herein is not to be construed as either an actual or implied endorsement of such products by the U.S. Department of Health and Human Services.

Data availability. Data underlying the results presented in this paper are available in Data File 1 [56], Data File 2 [57], Data File 3 [60], Data File 4 [62], Data File 5 [65] and Data File 6 [70].

Supplemental document. See Supplement 1 for supporting content.

References

1. S. A. Burns, A. E. Elsner, K. A. Sapoznik, R. L. Warner, and T. J. Gast, "Adaptive optics imaging of the human retina," Prog. Retinal Eye Res. **68**, 1–30 (2019).
2. J. Liang, D. R. Williams, and D. T. Miller, "Supernormal vision and high-resolution retinal imaging through adaptive optics," J. Opt. Soc. Am. A **14**(11), 2884–2892 (1997).
3. A. Roorda, F. Romero-Borja, W. Donnelly Iii, H. Queener, T. Hebert, and M. Campbell, "Adaptive optics scanning laser ophthalmoscopy," Opt. Express **10**(9), 405 (2002).
4. Y. Zhang, J. Rha, R. Jonnal, and D. Miller, "Adaptive optics parallel spectral domain optical coherence tomography for imaging the living retina," Opt. Express **13**(12), 4792 (2005).
5. D. T. Miller and K. Kurokawa, "Cellular scale imaging of transparent retinal structures and processes using adaptive optics optical coherence tomography," Annu. Rev. Vis. Sci. **6**(1), 115–148 (2020).
6. D. R. Williams, "Imaging single cells in the living retina," Vision Res. **51**(13), 1379–1396 (2011).
7. R. S. Jonnal, O. P. Kocaoglu, R. J. Zawadzki, Z. Liu, D. T. Miller, and J. S. Werner, "A review of adaptive optics optical coherence tomography: Technical advances, scientific applications, and the future," Invest. Ophthalmol. Visual Sci. **57**(9), OCT51 (2016).
8. M. Pircher and R. J. Zawadzki, "Review of adaptive optics OCT (AO-OCT): Principles and applications for retinal imaging [invited]," Biomed. Opt. Express **8**(5), 2536–2562 (2017).

Biomedical Optics EXPRESS

9. O. P. Kocaoglu, B. Cense, R. S. Jonnal, Q. Wang, S. Lee, W. Gao, and D. T. Miller, "Imaging retinal nerve fiber bundles using optical coherence tomography with adaptive optics," Vision Res. **51**(16), 1835–1844 (2011).
10. J. Tam, J. A. Martin, and A. Roorda, "Noninvasive visualization and analysis of parafoveal capillaries in humans," Invest. Ophthalmol. Visual Sci. **51**(3), 1691–1698 (2010).
11. A. Dubra, Y. Sulai, J. L. Norris, R. F. Cooper, A. M. Dubis, D. R. Williams, and J. Carroll, "Noninvasive imaging of the human rod photoreceptor mosaic using a confocal adaptive optics scanning ophthalmoscope," Biomed. Opt. Express **2**(7), 1864–1876 (2011).
12. J. I. Morgan, A. Dubra, R. Wolfe, W. H. Merigan, and D. R. Williams, "In vivo autofluorescence imaging of the human and macaque retinal pigment epithelial cell mosaic," Invest. Ophthalmol. Visual Sci. **50**(3), 1350–1359 (2009).
13. Z. Liu, O. P. Kocaoglu, and D. T. Miller, "3d imaging of retinal pigment epithelial cells in the living human retina," Invest. Ophthalmol. Visual Sci. **57**(9), OCT533 (2016).
14. T. Liu, H. Jung, J. Liu, M. Droettboom, and J. Tam, "Noninvasive near infrared autofluorescence imaging of retinal pigment epithelial cells in the human retina using adaptive optics," Biomed. Opt. Express **8**(10), 4348–4360 (2017).
15. C. E. Granger, Q. Yang, H. Song, K. Saito, K. Nozato, L. R. Latchney, B. T. Leonard, M. M. Chung, D. R. Williams, and E. A. Rossi, "Human retinal pigment epithelium: In vivo cell morphometry, multispectral autofluorescence, and relationship to cone mosaic," Invest. Ophthalmol. Visual Sci. **59**(15), 5705–5716 (2018).
16. Z. Liu, K. Kurokawa, F. Zhang, J. J. Lee, and D. T. Miller, "Imaging and quantifying ganglion cells and other transparent neurons in the living human retina," Proc. Natl. Acad. Sci. U. S. A. **114**(48), 12803–12808 (2017).
17. D. X. Hammer, A. Agrawal, R. Villanueva, O. Saeedi, and Z. Liu, "Label-free adaptive optics imaging of human retinal macrophage distribution and dynamics," Proc. Natl. Acad. Sci. U. S. A. **117**(48), 30661–30669 (2020).
18. J. V. Migacz, O. Otero-Marquez, R. Zhou, K. Rickford, B. Murillo, D. B. Zhou, M. V. Castanos, N. Sredar, A. Dubra, R. B. Rosen, and T. Y. P. Chui, "Imaging of vitreous cortex hyalocyte dynamics using non-confocal quadrant-detection adaptive optics scanning light ophthalmoscopy in human subjects," Biomed. Opt. Express **13**(3), 1755–1773 (2022).
19. A. Joseph, D. Power, and J. Schallek, "Imaging the dynamics of individual processes of microglia in the living retina in vivo," Biomed. Opt. Express **12**(10), 6157–6183 (2021).
20. K. Kurokawa, Z. Liu, and D. T. Miller, "Adaptive optics optical coherence tomography angiography for morphometric analysis of choriocapillaris [invited]," Biomed. Opt. Express **8**(3), 1803–1822 (2017).
21. H. Jung, T. Liu, J. Liu, L. A. Huryn, and J. Tam, "Combining multimodal adaptive optics imaging and angiography improves visualization of human eyes with cellular-level resolution," Commun. Biol. **1**(1), 189 (2018).
22. R. Sharma, D. R. Williams, G. Palczewska, K. Palczewski, and J. J. Hunter, "Two-photon autofluorescence imaging reveals cellular structures throughout the retina of the living primate eye," Invest. Ophthalmol. Visual Sci. **57**(2), 632 (2016).
23. J. E. McGregor, T. Godat, K. R. Dhakal, K. Parkins, J. M. Strazzeri, B. A. Bateman, W. S. Fischer, D. R. Williams, and W. H. Merigan, "Optogenetic restoration of retinal ganglion cell activity in the living primate," Nat. Commun. **11**(1), 1703 (2020).
24. E. A. Rossi, C. E. Granger, R. Sharma, Q. Yang, K. Saito, C. Schwarz, S. Walters, K. Nozato, J. Zhang, T. Kawakami, W. Fischer, L. R. Latchney, J. J. Hunter, M. M. Chung, and D. R. Williams, "Imaging individual neurons in the retinal ganglion cell layer of the living eye," Proc. Natl. Acad. Sci. U. S. A. **114**(3), 586–591 (2017).
25. K. A. Sapoznik, T. Luo, A. de Castro, L. Sawides, R. L. Warner, and S. A. Burns, "Enhanced retinal vasculature imaging with a rapidly configurable aperture," Biomed. Opt. Express **9**(3), 1323–1333 (2018).
26. D. Scoles, Y. N. Sulai, C. S. Langlo, G. A. Fishman, C. A. Curcio, J. Carroll, and A. Dubra, "In vivo imaging of human cone photoreceptor inner segments," Invest. Ophthalmol. Visual Sci. **55**(7), 4244–4251 (2014).
27. C. E. Bigelow, N. V. Iftimia, R. D. Ferguson, T. E. Ustun, B. Bloom, and D. X. Hammer, "Compact multimodal adaptive-optics spectral-domain optical coherence tomography instrument for retinal imaging," J. Opt. Soc. Am. A **24**(5), 1327 (2007).
28. S. A. Burns, R. Tumbar, A. E. Elsner, D. Ferguson, and D. X. Hammer, "Large-field-of-view, modular, stabilized, adaptive-optics-based scanning laser ophthalmoscope," J. Opt. Soc. Am. A **24**(5), 1313–1326 (2007).
29. D. X. Hammer, R. D. Ferguson, M. Mujat, A. Patel, E. Plumb, N. Iftimia, T. Y. Chui, J. D. Akula, and A. B. Fulton, "Multimodal adaptive optics retinal imager: Design and performance," J. Opt. Soc. Am. A **29**(12), 2598 (2012).
30. Z. Liu, J. Tam, O. Saeedi, and D. X. Hammer, "Trans-retinal cellular imaging with multimodal adaptive optics," Biomed. Opt. Express **9**(9), 4246–4262 (2018).
31. E. M. Wells-Gray, S. S. Choi, R. J. Zawadzki, S. C. Finn, C. Greiner, J. S. Werner, and N. Doble, "Volumetric imaging of rod and cone photoreceptor structure with a combined adaptive optics-optical coherence tomography-scanning laser ophthalmoscope," J. Biomed. Opt. **23**(3), 1–15 (2018).
32. A. J. Bower, T. Liu, N. Aguilera, J. Li, J. Liu, R. Lu, J. P. Giannini, L. A. Huryn, A. Dubra, Z. Liu, D. X. Hammer, and J. Tam, "Integrating adaptive optics-slo and oct for multimodal visualization of the human retinal pigment epithelial mosaic," Biomed. Opt. Express **12**(3), 1449–1466 (2021).
33. T. Klein, W. Wieser, L. Reznicek, A. Neubauer, A. Kampik, and R. Huber, "Multi-MHz retinal OCT," Biomed. Opt. Express **4**(10), 1890 (2013).
34. M. Azimipour, R. S. Jonnal, J. S. Werner, and R. J. Zawadzki, "Coextensive synchronized slo-oct with adaptive optics for human retinal imaging," Opt. Lett. **44**(17), 4219–4222 (2019).

Biomedical Optics EXPRESS

35. M. Azimipour, J. V. Migacz, R. J. Zawadzki, J. S. Werner, and R. S. Jonnal, "Functional retinal imaging using adaptive optics swept-source oct at 1.6 mhz," Optica **6**(3), 300–303 (2019).
36. M. Azimipour, D. Valente, K. V. Vienola, J. S. Werner, R. J. Zawadzki, and R. S. Jonnal, "Optoretinogram: Optical measurement of human cone and rod photoreceptor responses to light," Opt. Lett. **45**(17), 4658–4661 (2020).
37. V. P. Pandiyan, X. Jiang, J. A. Kuchenbecker, and R. Sabesan, "Reflective mirror-based line-scan adaptive optics oct for imaging retinal structure and function," Biomed. Opt. Express **12**(9), 5865–5880 (2021).
38. M. Laslandes, M. Salas, C. K. Hitzenberger, and M. Pircher, "Increasing the field of view of adaptive optics scanning laser ophthalmoscopy," Biomed. Opt. Express **8**(11), 4811–4826 (2017).
39. P. Mecê, J. Scholler, K. Groux, K. Grieve, and C. Boccara, "Adaptive glasses wavefront sensorless full-field oct for high-resolution retinal imaging over a wide field-of-view," *SPIE Photonics West 2021 - SPIE BiOS*, Mar 2021, Online Only, United States, pp.1162306, ff10.1117/12.2576689ff. ffhal-03165160f (2021).
40. M. Paques, S. Meimon, F. Rossant, D. Rosenbaum, S. Mrejen, F. Sennlaub, and K. Grieve, "Adaptive optics ophthalmoscopy: Application to age-related macular degeneration and vascular diseases," Prog. Retinal Eye Res. **66**, 1–16 (2018).
41. K. Sambhav, S. Grover, and K. V. Chalam, "The application of optical coherence tomography angiography in retinal diseases," Surv. Ophthalmol. **62**(6), 838–866 (2017).
42. R. S. Jonnal, O. P. Kocaoglu, Q. Wang, S. Lee, and D. T. Miller, "Phase-sensitive imaging of the outer retina using optical coherence tomography and adaptive optics," Biomed. Opt. Express **3**(1), 104 (2012).
43. D. Hillmann, H. Spahr, C. Pfaffle, H. Sudkamp, G. Franke, and G. Huttmann, "In vivo optical imaging of physiological responses to photostimulation in human photoreceptors," Proc. Natl. Acad. Sci. U. S. A. **113**(46), 13138–13143 (2016).
44. F. Zhang, K. Kurokawa, A. Lassoued, J. A. Crowell, and D. T. Miller, "Cone photoreceptor classification in the living human eye from photostimulation-induced phase dynamics," Proc. Natl. Acad. Sci. U. S. A. **116**(16), 7951–7956 (2019).
45. V. P. Pandiyan, A. Maloney-Bertelli, J. A. Kuchenbecker, K. C. Boyle, T. Ling, Z. C. Chen, B. H. Park, A. Roorda, D. Palanker, and R. Sabesan, "The optoretinogram reveals the primary steps of phototransduction in the living human eye," Sci. Adv. **6**(37), eabc1124 (2020).
46. R. F. Cooper, D. H. Brainard, and J. I. W. Morgan, "Optoretinography of individual human cone photoreceptors," Opt. Express **28**(26), 39326–39339 (2020).
47. A. Lassoued, F. Zhang, K. Kurokawa, Y. Liu, M. T. Bernucci, J. A. Crowell, and D. T. Miller, "Cone photoreceptor dysfunction in retinitis pigmentosa revealed by optoretinography," Proc. Natl. Acad. Sci. U. S. A. **118**(47), e2107444118 (2021).
48. Z. Liu, K. Kurokawa, D. X. Hammer, and D. T. Miller, "In vivo measurement of organelle motility in human retinal pigment epithelial cells," Biomed. Opt. Express **10**(8), 4142–4158 (2019).
49. C. Pfaffle, H. Spahr, L. Kutzner, S. Burhan, F. Hilge, Y. Miura, G. Huttmann, and D. Hillmann, "Simultaneous functional imaging of neuronal and photoreceptor layers in living human retina," Opt. Lett. **44**(23), 5671–5674 (2019).
50. A. Dubra and Y. Sulai, "Reflective afocal broadband adaptive optics scanning ophthalmoscope," Biomed. Opt. Express **2**(6), 1757–1768 (2011).
51. J. P. Kolb, W. Draxinger, J. Klee, T. Pfeiffer, M. Eibl, T. Klein, W. Wieser, and R. Huber, "Live video rate volumetric oct imaging of the retina with multi-mhz a-scan rates," PLoS One **14**(3), e0213144 (2019).
52. ANSI, "Z80.36 American National Standard for Ophthalmic - Light Hazard Protection For Ophthalmic Instruments," (2016).
53. A. Agrawal, T. J. Pfefer, P. D. Woolliams, P. H. Tomlins, and G. Nehmetallah, "Methods to assess sensitivity of optical coherence tomography systems," Biomed. Opt. Express **8**(2), 902–917 (2017).
54. W. A. Rushton and G. H. Henry, "Bleaching and regeneration of cone pigments in man," Vision Res. **8**(6), 617 (1968).
55. A. Mariampillai, B. A. Standish, E. H. Moriyama, M. Khurana, N. R. Munce, M. K. Leung, J. Jiang, A. Cable, B. C. Wilson, I. A. Vitkin, and V. X. Yang, "Speckle variance detection of microvasculature using swept-source optical coherence tomography," Opt. Lett. **33**(13), 1530 (2008).
56. Z. Liu, F. Zhang, K. Zucca, A. Agrawal, and D. X. Hammer, "Data file 1," figshare, 2022, https://doi.org/10.6084/m9.figshare.19669053.
57. Z. Liu, F. Zhang, K. Zucca, A. Agrawal, and D. X. Hammer, "Data file 2," figshare, 2022, https://doi.org/10.6084/m9.figshare.19669038.
58. S. Soltanian-Zadeh, K. Kurokawa, Z. Liu, D. X. Hammer, D. T. Miller, and S. Farsiu, "Fully automatic quantification of individual ganglion cells from A0-OCT volumes via weakly supervised learning," Proc. SPIE **11218**, 112180Q (2020).
59. Z. Liu, O. Saeedi, F. Zhang, R. Villanueva, S. Asanad, A. Agrawal, and D. X. Hammer, "Quantification of retinal ganglion cell morphology in human glaucomatous eyes," Invest. Ophthalmol. Visual Sci. **62**(3), 34 (2021).
60. Z. Liu, F. Zhang, K. Zucca, A. Agrawal, and D. X. Hammer, "Data file 2," figshare, 2022, https://doi.org/10.6084/m9.figshare.19669047.
61. D. X. Hammer, Z. Liu, K. Kovalick, O. Saeedi, and D. Harrison, "Adaptive optics – optical coherence tomography imaging of the inner retina in multiple sclerosis," Photonics West, Ophthalmic Technologies XXXII 11941-8 (2022).

Biomedical Optics EXPRESS

62. Z. Liu, F. Zhang, K. Zucca, A. Agrawal, and D.X. Hammer, "Data file 4," figshare, 2022, https://doi.org/10.6084/m9.figshare.19669041.
63. H. Song, T. Y. Chui, Z. Zhong, A. E. Elsner, and S. A. Burns, "Variation of cone photoreceptor packing density with retinal eccentricity and age," Invest. Ophthalmol. Visual Sci. **52**(10), 7376 (2011).
64. Z. Liu, O. P. Kocaoglu, T. L. Turner, and D. T. Miller, "Modal content of living human cone photoreceptors," Biomed. Opt. Express **6**(9), 3378 (2015).
65. Z. Liu, F. Zhang, K. Zucca, A. Agrawal, and D. X. Hammer, "Data file 5," figshare, 2022, https://doi.org/10.6084/m9.figshare.19669044.
66. A. H. Kashani, C. L. Chen, J. K. Gahm, F. Zheng, G. M. Richter, P. J. Rosenfeld, Y. Shi, and R. K. Wang, "Optical coherence tomography angiography: A comprehensive review of current methods and clinical applications," Prog. Retinal Eye Res. **60**, 66–100 (2017).
67. J. V. Migacz, I. Gorczynska, M. Azimipour, R. Jonnal, R. J. Zawadzki, and J. S. Werner, "Megahertz-rate optical coherence tomography angiography improves the contrast of the choriocapillaris and choroid in human retinal imaging," Biomed. Opt. Express **10**(1), 50–65 (2019).
68. E. Auksorius, D. Borycki, P. Wegrzyn, B.L. Sikorski, I. Zickiene, K. Lizewski, M. Rapolu, K. Adomavicius, S. Tomczewski, and M. Wojtkowski, "Spatio-temporal optical coherence tomography provides advanced imaging of the human retina and choroid," arXiv 2107.10672 (2021).
69. M. Salas, M. Augustin, L. Ginner, A. Kumar, B. Baumann, R. Leitgeb, W. Drexler, S. Prager, J. Hafner, U. Schmidt-Erfurth, and M. Pircher, "Visualization of micro-capillaries using optical coherence tomography angiography with and without adaptive optics," Biomed. Opt. Express **8**(1), 207–222 (2017).
70. Z. Liu, F. Zhang, K. Zucca, A. Agrawal, and D. X. Hammer, "Data file 6," figshare, 2022, https://doi.org/10.6084/m9.figshare.19669050
71. F. Felberer, J. S. Kroisamer, B. Baumann, S. Zotter, U. Schmidt-Erfurth, C. K. Hitzenberger, and M. Pircher, "Adaptive optics slo/oct for 3d imaging of human photoreceptors in vivo," Biomed. Opt. Express **5**(2), 439–456 (2014).
72. D. Valente, K. V. Vienola, R. J. Zawadzki, and R. S. Jonnal, "Kilohertz retinal FF-SS-OCT and flood imaging with hardware-based adaptive optics," Biomed. Opt. Express **11**(10), 5995–6011 (2020).
73. Y. Miao, M. Siadati, J. Song, D. Ma, Y. Jian, M. F. Beg, M. V. Sarunic, and M. J. Ju, "Phase-corrected buffer averaging for enhanced oct angiography using fdml laser," Opt. Lett. **46**(16), 3833–3836 (2021).
74. B. Braaf, K. A. Vermeer, K. V. Vienola, and J. F. de Boer, "Angiography of the retina and the choroid with phase-resolved OCT using interval-optimized backstitched b-scans," Opt. Express **20**(18), 20516–34 (2012).
75. R. J. Zawadzki, B. Cense, Y. Zhang, S. S. Choi, D. T. Miller, and J. S. Werner, "Ultrahigh-resolution optical coherence tomography with monochromatic and chromatic aberration correction," Opt. Express **16**(11), 8126 (2008).